

Article

# Mapping Multiple Insect Outbreaks across Large Regions Annually Using Landsat Time Series Data

Benjamin C. Bright <sup>1,\*</sup> , Andrew T. Hudak <sup>1</sup> , Arjan J.H. Meddens <sup>2</sup>, Joel M. Egan <sup>3</sup> and Carl L. Jorgensen <sup>4</sup> 

<sup>1</sup> Rocky Mountain Research Station, United States Forest Service, 1221 South Main Street, Moscow, ID 83843, USA; andrew.hudak@usda.gov

<sup>2</sup> School of the Environment, Washington State University, PO Box 642812, Pullman, WA 99164, USA; arjan.meddens@wsu.edu

<sup>3</sup> Northern Region, Forest Health Protection, United States Forest Service, 26 Fort Missoula Road, Missoula, MT 59804, USA; joel.egan@usda.gov

<sup>4</sup> Intermountain Regions, Forest Health Protection, United States Forest Service, 1249 Vinnell Way, Suite 200, Boise, ID 83709, USA; carl.jorgensen@usda.gov

\* Correspondence: benjamin.c.bright@usda.gov; Tel.: +1-208-883-2311

Received: 27 April 2020; Accepted: 19 May 2020; Published: 21 May 2020



**Abstract:** Forest insect outbreaks have caused and will continue to cause extensive tree mortality worldwide, affecting ecosystem services provided by forests. Remote sensing is an effective tool for detecting and mapping tree mortality caused by forest insect outbreaks. In this study, we map insect-caused tree mortality across three coniferous forests in the Western United States for the years 1984 to 2018. First, we mapped mortality at the tree level using field observations and high-resolution multispectral imagery collected in 2010, 2011, and 2018. Using these high-resolution maps of tree mortality as reference images, we then classified moderate-resolution Landsat imagery as disturbed or undisturbed and for disturbed pixels, predicted percent tree mortality with random forest (RF) models. The classification approach and RF models were then applied to time series of Landsat imagery generated with Google Earth Engine (GEE) to create annual maps of percent tree mortality. We separated disturbed from undisturbed forest with overall accuracies of 74% to 80%. Cross-validated RF models explained 61% to 68% of the variation in percent tree mortality within disturbed 30-m pixels. Landsat-derived maps of tree mortality were comparable to vector aerial survey data for a variety of insect agents, in terms of spatial patterns of mortality and annual estimates of total mortality area. However, low-level tree mortality was not always detected. We conclude that our methodology has the potential to generate reasonable estimates of annual tree mortality across large extents.

**Keywords:** forest; insects; bark beetles; defoliators; tree mortality; Landsat; time series; mapping

## 1. Introduction

Forest insect outbreaks have caused widespread tree mortality worldwide in recent years [1]. Although insect-caused tree mortality has been ongoing for millennia [2], recent climate conditions have facilitated insect outbreaks by increasing tree vulnerability and altering insect population dynamics [1,3–5]. Extensive tree mortality caused by insect outbreaks affects crucial ecosystem services provided by forests such as water supply [6,7], carbon storage [8], wildlife habitat [9], and the availability of forest products [10]. Accurate estimates of the extent and severity of insect-caused tree mortality are important for determining to what degree ecosystem services have been affected [11–13]. In this study, we demonstrate a methodology for mapping insect-caused tree mortality annually across large extents using Landsat time series analysis.

The United States Department of Agriculture (USDA) Forest Service and partner agencies conduct annual insect and disease surveys (IDS) to monitor insect activity across the nation's forests. Surveyors aboard fixed-wing aircraft estimate the spatial extent, insect mortality agent, tree species host, and severity of insect-caused tree damage. IDS data are not only useful for monitoring and anticipating future insect-caused tree mortality [14,15], but are also valuable for research applications investigating the causes and effects of forest insect outbreaks e.g., [8,16,17]. However, IDS data accuracy is limited; surveyors only have a short time to estimate often extensive tree damage; surveying conditions can be less than ideal; surveyor experience can influence accuracy; and some areas such as wilderness are surveyed only infrequently, leading to data gaps [18]. In addition, IDS data coverage might become less extensive in the future than recent years as costs increase and budgets decrease; therefore, the USDA Forest Health Protection program responsible for overseeing IDS is making efforts to incorporate satellite remote sensing in future forest health monitoring [19].

Satellite imagery is becoming a logical alternative to aerial surveys for monitoring and mapping insect-caused tree mortality. Landsat satellites, with moderate spatial resolutions of 30 m and temporal revisit times of 16 days, are particularly well-suited for this task. Furthermore, the Landsat TM mission of satellites has been in operation since 1984, making it possible to perform long-term time series analyses. Several algorithms have been developed for detecting general forest change through time with Landsat time series analysis [20]; these algorithms include Vegetation Change Tracker (VCT) [21], Landsat-based detection of Trends in Disturbance and Recovery (LandTrendr) [22], Breaks for Additive Seasonal and Trend (BFAST) [23], and Continuous Change Detection and Classification (CCDC) [24]. Google Earth Engine (GEE) has recently made the application of such algorithms more accessible to users [25]; for instance, the LandTrendr algorithm and associated Landsat preprocessing tasks have been implemented in GEE [26].

Previous work has shown how Landsat time series analysis can be used to estimate continuous levels (i.e., percent of a 30-m pixel) of severe insect-related forest disturbances (see Senf et al. [27] for a review). Meigs et al. [28] showed that LandTrendr was sensitive to continuous levels of defoliator and bark beetle damage in Oregon, USA. Townsend et al. [29] developed models predicting canopy defoliation severity in broadleaf deciduous forests in the eastern USA. Meddens et al. [30] and Meddens and Hicke [31] demonstrated a methodology for predicting continuous mountain pine beetle damage through time in Colorado, USA; in this methodology, tree mortality is mapped using high-resolution satellite imagery, which is then used to 1) classify forested Landsat pixels as disturbed or undisturbed, and 2) predict the continuous percent tree mortality of disturbed pixels. Assal et al. [32] and Long and Lawrence [33] followed a similar approach to Meddens and Hicke [31] to estimate continuous mountain pine beetle-caused tree mortality in Montana, USA. Meigs et al. [34] predicted and mapped bark beetle and defoliator damage in terms of basal area across Oregon and Washington, USA. Woodward et al. [35] used a time series of Landsat data to map tree mortality severity caused by spruce beetles in Colorado, USA. Most previous studies have demonstrated the use of Landsat imagery for predicting mountain pine beetle-caused tree mortality; more studies are needed that demonstrate the use of Landsat image time series for predicting continuous tree mortality caused by other mortality agents.

To extend the work of Meddens et al. [30] and Meddens and Hicke [31], we investigated how their methodology performed in three additional study areas in the Western United States that have experienced tree mortality caused by a variety of mortality agents. Our approach differed from that of Meddens et al. [30] and Meddens and Hicke [31] in that we (1) used GEE [25] to generate Landsat image time series and implement the algorithm of Meddens and Hicke [31]; and (2) we used Random Forest (RF) modeling rather than linear modeling to predict continuous tree mortality. We conclude that the methodology of Meddens et al. [30] and Meddens and Hicke [31], implemented within GEE, provides an effective means for mapping insect-caused tree mortality annually across large spatial extents.

## 2. Materials and Methods

### 2.1. Study Areas

We chose three areas in the Western United States where insect activity has been elevated in recent years, and where classified high-resolution multispectral imagery was available. Study areas included the 1) Stanley, Idaho vicinity, 2) Chimney Park, Wyoming vicinity, and 3) Elk City, Idaho vicinity (Figure 1). The forest around both Stanley and Chimney Park is dominated by lodgepole pine (*Pinus contorta* Douglas ex Loudon), with Douglas-fir (*Pseudotsuga menziesii* (Mirb.) Franco) and ponderosa pine (*Pinus ponderosa* Lawson and C. Lawson) occurring at lower elevations, and Engelmann spruce (*Picea engelmannii* Parry ex Engelm.), subalpine fir (*Abies lasiocarpa* (Hook.) Nutt.), limber pine (*Pinus flexilis* James), and whitebark pine (*Pinus albicaulis* Engelm.) occurring at higher elevations. The forest around Elk City is mixed-conifer consisting of grand fir (*Abies grandis* (Douglas ex D. Don) Lindl.), Douglas-fir, ponderosa pine, lodgepole pine, Western white pine (*Pinus monticola* (Douglas ex D. Don)), Western larch (*Larix occidentalis* Nutt.), Engelmann spruce, and subalpine fir.

Mountain pine beetle (*Dendroctonus ponderosae* Hopkins) outbreaks began in 2000 and 2005 in the Stanley and Chimney Park study areas, respectively. Other prominent mortality agents in the Stanley and Chimney Park study areas include Western spruce budworms (*Choristoneura occidentalis* Freeman) in Douglas-fir and subalpine fir, Douglas-fir beetles (*Dendroctonus pseudotsugae* Hopkins) in Douglas-fir, and spruce beetles (*Dendroctonus rufipennis* Kirby) in Engelmann spruce. In the Elk City study area, insect activity has been elevated for many years and includes several mortality agents: mountain pine beetles in lodgepole pine, Douglas-fir beetles in Douglas-fir, fir engravers (*Scolytus ventralis* LeConte) in grand fir, spruce beetles in Engelmann spruce, Western pine beetles (*Dendroctonus brevicomis* LeConte) in ponderosa pine, Western balsam bark beetles (*Dryocoetes confuses* Swaine) in subalpine fir, and balsam woolly adelgids (*Adelges piceae* (Ratzeburg)) in grand and subalpine fir.

Terrain is generally mountainous in all study areas with elevations that range from 1080 to 3270, 2000 to 4140, and 370 to 2710 m above sea level for the Stanley, Chimney Park, and Elk City study areas, respectively. Temperature averages 2.0, 2.7, and 3.8 °C, and annual precipitation averages 654, 381, and 800 mm for the Stanley, Chimney Park, and Elk City study areas, respectively (1961 to 1990) [36].

### 2.2. Field Observations

Field observations of live and beetle-killed trees in the Stanley and Elk City study areas were gathered in the summers of 2010 and 2018, respectively. Field observations were not gathered in the Chimney Park study area. As part of a previous project [37], we stratified the Stanley study area by biomass using pre-outbreak NDVI to sample in a variety of forest conditions. The Elk City study area was stratified by mortality severity and agent using 2017 to 2018 IDS data, to ensure sampling across a range of mortality conditions and agents [38]. In both study areas, we located plot centers following stratified random sampling designs, and navigated to plot centers with professional-grade Trimble GNSS receivers in the field.

At plot centers, we established circular 400 m<sup>2</sup> fixed-radius plots (radii of 11.3 m) and measured all trees within plot extents with a diameter at breast height (DBH) >7 cm and >10 cm in Stanley and Elk City, respectively. In addition to DBH, we measured tree condition (live or dead), species, canopy dominance, mortality agent, estimated time since death (based on needle, branch, and bole condition, see Bright et al. [38], Table A1) or how many needles were remaining on dead trees, and distance and bearing from plot center. We logged several hundred positions at plot centers using the GNSS receivers, and differentially corrected plot center locations so that estimated plot center accuracies were <1 m. Plot center locations along with distance and bearing measurements were used to calculate individual tree locations, which were then used to select pixels for image classification.

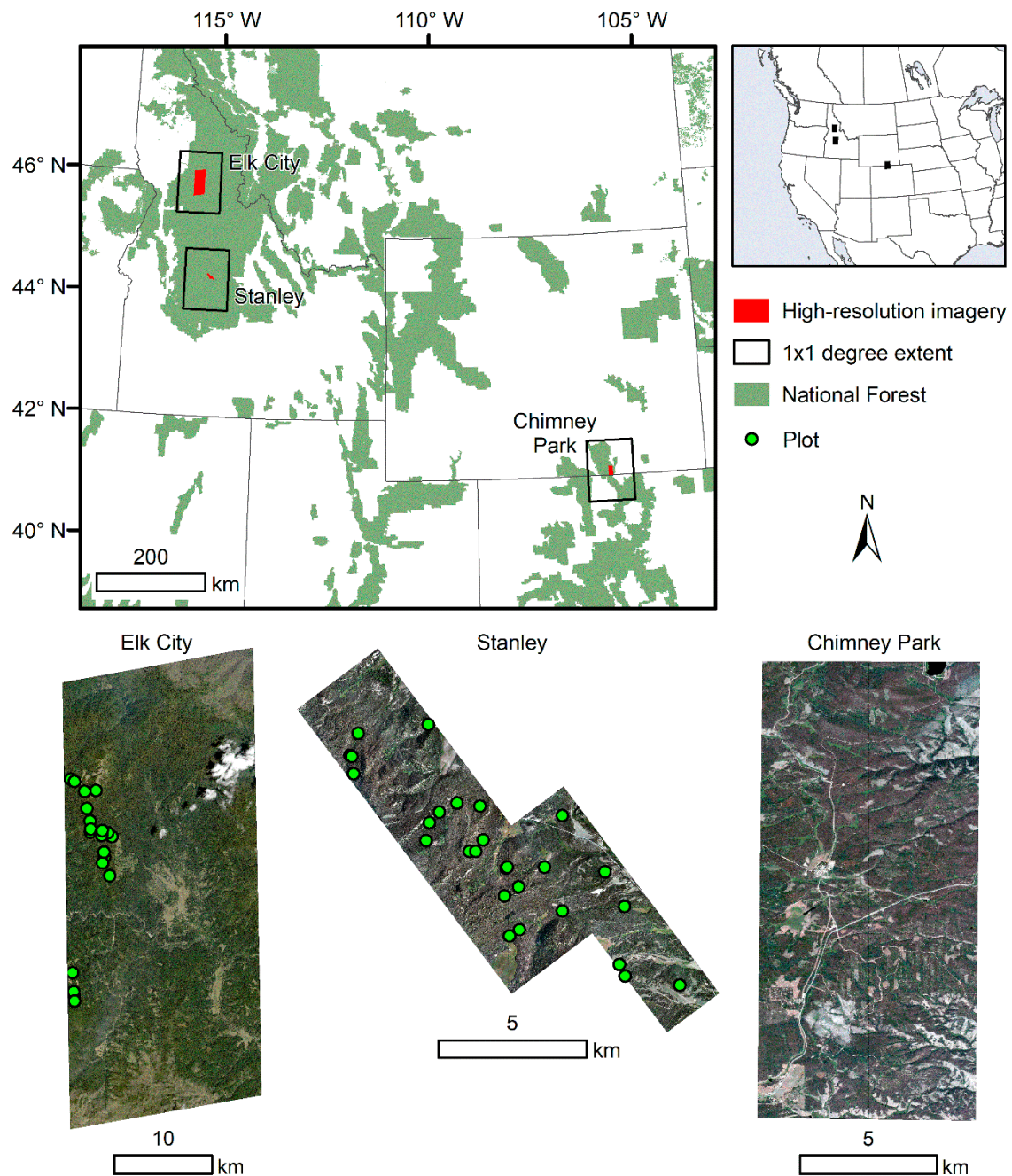


**Figure 1.** Study areas near Elk City and Stanley, Idaho, and Chimney Park, Wyoming, United States. Models predicting percent tree mortality were developed in areas of high-resolution multispectral imagery. Models were then applied to time series of Landsat imagery within  $1 \times 1$  degree extents.

### 2.3. High-Resolution and Landsat Imagery

High-resolution multispectral imagery was acquired over the Stanley, Chimney Park, and Elk City study areas in 2010, 2011, and 2018, respectively (Figure 1). High-resolution imagery characteristics varied by study area (Table 1). Imagery of the Stanley study area consisted of digital aerial orthophotography, whereas Chimney Park and Elk City imagery came from the QuickBird and WorldView-2 satellites. Landsat imagery was processed in and acquired from the LandTrendr implementation in GEE, which uses USGS Landsat Surface Reflectance Tier 1 imagery data sets.

**Table 1.** Characteristics of high-resolution multispectral imagery for each area.

Study Area	Platform	Date	Spatial Resolution (m)	Number of Bands	Area (ha)
Stanley	Fixed-wing aircraft	Aug. 2010	0.2	4	6432
Chimney Park	QuickBird	Aug. 2011	2.4	4	13,600
Elk City	WorldView-2	Sept. 2018	2	8	104,896

#### 2.4. Imagery Processing

In each of the three study areas, high-resolution imagery was used to create maps of tree mortality, which were then aggregated to a spatial resolution of 30-m, and used as reference data to (1) classify Landsat imagery as non-forest, disturbed forest and undisturbed forest, and (2) predict percent tree mortality of disturbed pixels (Figure 2). Models predicting percent tree mortality were then applied to Landsat time series spanning the years 1984 to 2018. Each of these steps are described in more detail below.

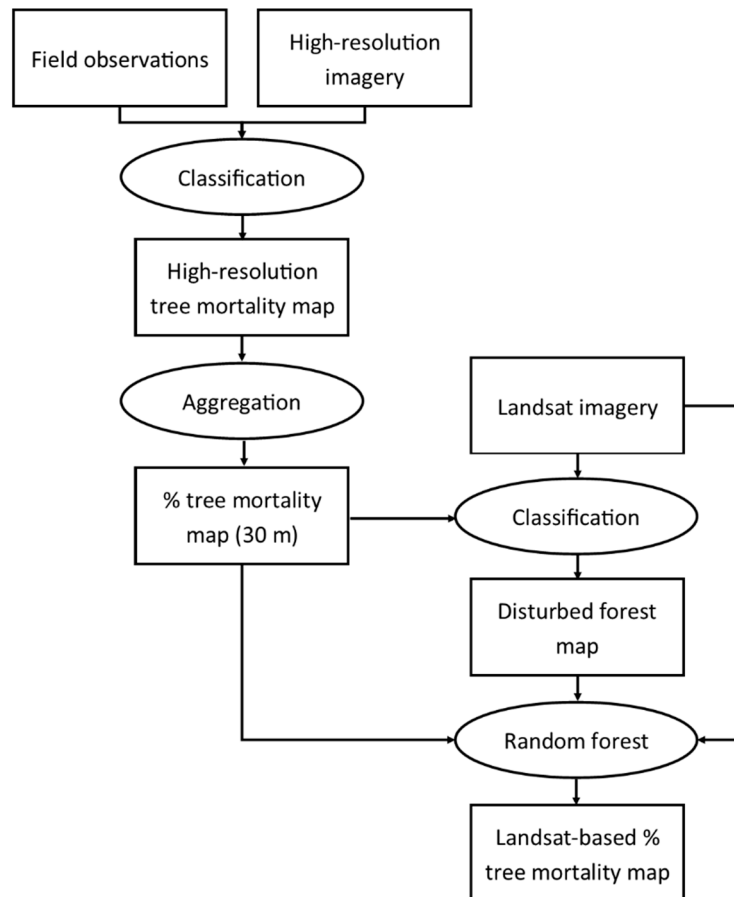


**Figure 2.** Overview of how field observations, high-resolution imagery, and Landsat imagery were used to create maps of percent tree mortality. This process was repeated for each of the three study areas.

##### 2.4.1. High-Resolution Multispectral Imagery Processing

Image classification routines for each study area resulted in the separation of beetle-killed trees from live trees. The routines all used maximum likelihood classification and similar classification variables, including the Normalized Difference Vegetation Index (NDVI) and Red-Green Index (RGI), which are defined as:

$$NDVI = (NIR - RED) / (NIR + RED), \quad (1)$$

$$RGI = RED / GREEN, \quad (2)$$

where *NIR* is the near-infrared band, *RED* is the red band, and *GREEN* is the green band. Classification accuracy was evaluated using confusion matrices and visual comparison with true-color imagery.

For details on the classification of the Stanley aerial orthoimagery, see Bright et al. [37]. Briefly here, digital aerial orthoimagery was aggregated by averaging 0.2-m pixels to a spatial resolution of 2.4 m, the approximate average crown area of canopy trees in the imagery extent; aggregating imagery to 2.4 m pixels increased classification accuracy by reducing confusion between sunlit and shadowed tree crowns [39]. Sixteen-bit digital numbers (DN) were divided by 65,535 so that pixel values ranged from 0 to 1. Field observations were used to identify live and beetle-killed tree pixels on aggregated imagery. Two-thirds of the identified pixels were used for classification training; the remaining third were used for classification evaluation. Classification consisted of several steps: (1) water was classified using the NIR band ( $NIR < 0.15$  indicated water); (2) shadows were separated from non-shadow pixels using the RED band ( $RED < 0.15$  indicated shadow); (3) a canopy height model (CHM) derived from coincident light detection and ranging data (lidar) was used separate forest and non-forest ( $CHM < 0.5$  m indicated non-forest); (4) pixels with a  $RGI > 1.08$  were classified as newly-killed red trees, and the remaining pixels were classified as either green or gray trees using NIR, NDVI, and RGI in a maximum likelihood classifier. Water, shadow, and red tree thresholds were determined from visual inspection of true- and false-color imagery [37,39]. Overall lifeform classification accuracy was 87%.

The Chimney Park QuickBird satellite imagery was classified similarly to the Stanley imagery, except no field observations were available for calibration/evaluation. DNs in 11 bits were divided by 2048 to convert pixels to values between 0 and 1. The topography of the Chimney Park study area is relatively flat; healthy trees and red and gray beetle-killed tree pixels were easily identified on true- and false-color QuickBird imagery (Figure 1). Pixels of green and brown herbaceous cover and non-vegetated surfaces such as bare soil and road were also identified on imagery. Six hundred pixels of each class were identified across the image; half were used for classification training and half for evaluation. Water and shadow pixels were classified with threshold values of  $NIR < 0.07$  and  $RED < 0.04$ , respectively, and the remainder of classes were classified in a maximum likelihood classifier using GREEN, NDVI, and RGI as classification variables. Overall lifeform classification accuracy was 97%.

Elk City WorldView-2 imagery was delivered as a standard (2A) product, which had been orthorectified using a coarse digital elevation model (DEM). Imagery appeared to be well-corrected for terrain when compared with high-resolution orthoimagery. Imagery was converted from DNs to top-of-atmosphere (TOA) reflectance using equations recommended by DigitalGlobe [40]. TOA reflectance imagery was then converted to surface reflectance using empirical line calibration [41,42]. We selected live and dead tree pixels on imagery using field-measured tree locations. Visual inspection of imagery was used to select pixels of green and brown herbaceous cover, as well as non-vegetated surfaces. Half of the pixels were used for classification training; the remainder were used for classification evaluation. Imagery was classified using the GREEN, red-edge (WV2 band 6), NIR (WV2 band 8), NDVI, and RGI as classification variables in a maximum likelihood classifier. Shadows were masked with the RED band ( $RED < 4.1\%$  indicated shadow). Overall lifeform classification accuracy was 96%.

High-resolution classifications for each study area were then aggregated to 30-m grids to be used for comparison with Landsat imagery. We created a mode aggregation grid for each study area, where aggregated 30-m pixels took the value of the modal class, as well as grids of percent area by class, including percent dead tree grids to be used as response variables in predictive models.

#### 2.4.2. Landsat Imagery Processing

Annual Landsat image time series for the years 1984 to 2018 coincident with high-resolution imagery were created using functions from the LandTrendr implementation in GEE [25,26].

Newer Landsat-8 OLI imagery (launched in 2013) differs spectrally from older Landsat-5 TM and Landsat-7 ETM+ imagery. To account for this difference when building imagery time series that include both older and newer Landsat-8 OLI imagery, the LandTrendr implementation in GEE transforms Landsat-8 OLI bands to Landsat-7 ETM+ band equivalents using the equations of Roy et al. [43] (Table 2). Using the ‘buildSRcollection’ function, we created annual median (value closest to the median) composite images of surface reflectance for the years 1984 to 2018 from cloud-, shadow-, and snow-free imagery between the dates of June 20 and September 20. Annual time series of individual bands and indices were then created using the ‘transformSRcollection’ and ‘collectionToBandStack’ functions (Table 2). Note that we did not run the LandTrendr algorithm on our time series data to identify disturbed pixels, but rather used the algorithm of Meddens and Hicke [31], which we describe below. We chose to use the preprocessing routines available in the LandTrendr implementation of GEE because we found them to be well-documented and straightforward.

**Table 2.** Bands and spectral indices for which annual time series were created. Variables were used for classification and as candidate variables in Random Forest models predicting percent tree mortality.

Band or Index	Description	Formula
B1	Band 1 (Landsat TM equivalent)	
B2	Band 2 (Landsat TM equivalent)	
B3	Band 3 (Landsat TM equivalent)	
B4	Band 4 (Landsat TM equivalent)	
B5	Band 5 (Landsat TM equivalent)	
B6	Band 6 (Landsat TM equivalent)	
B7	Band 7 (Landsat TM equivalent)	
NBR	Normalized Burn Ratio	$(B4 - B7)/(B4 + B7)$
NDVI	Normalized Difference Vegetation Index	$(B4 - B3)/(B4 + B3)$
TCB	Tasseled-Cap Brightness	$0.2043*B1 + 0.4158*B2 + 0.5524*B3$ $+ 0.5741*B4 + 0.3124*B5 + 0.2303*B7$
TCG	Tasseled-Cap Greenness	$-0.1603*B1 - 0.2819*B2 - 0.4934*B3$ $+ 0.7940*B4 - 0.0002*B5 - 0.1446*B7$
TCW	Tasseled-Cap Wetness	$0.0315*B1 + 0.2021*B2 + 0.3102*B3$ $+ 0.1594*B4 - 0.6806*B5 - 0.6109*B7$
B54A	Band 5/Band 4 anomaly from undisturbed mean	$B54 - \overline{B54}_{undist.}$
NBRA	Normalized Burn Ratio anomaly from undisturbed mean	$NBR - \overline{NBR}_{undist.}$

The iterative method of Meddens et al. [30] was used to create time series of B5/B4 and NBR anomalies from undisturbed means (B54A, NBRA). To create undisturbed mean B5/B4 and NBR images, mean images of B5/B4 and NBR for all years (1984–2018) were created; pixels that were more than one standard deviation from means in the direction of disturbances (positive for B5/B4 and negative for NBR) were identified as disturbed pixels, and mean images without disturbed pixels were recalculated. This process was repeated 10 times until means stabilized to create undisturbed mean B5/B4 and NBR images. One assumption of this approach is that forested pixels were undisturbed some time during the years 1984 to 2018.

Time series of B54A and NBRA for the years 1984 to 2018 were then created by subtracting undisturbed mean B5/B4 and NBR images from annual B5/B4 and NBR images, respectively. B54A and NBRA were used for classification of predominantly live (undisturbed) or predominantly dead (disturbed) tree cover; B54A was also used as a candidate predictor variable in models predicting percent mortality. Landsat imagery preprocessing was performed in GEE, and output from GEE for classification and predictive modeling analysis in R [44].

### 2.5. Landsat Classification

Following the classification method of Meddens et al. [30], we created a classification of non-forest, disturbed forest, and undisturbed forest for each of the three study areas. Landsat classifications were created for the years that corresponded to high-resolution imagery years; 2010, 2011, and 2018 for the Stanley, Chimney Park, and Elk City study areas, respectively. Forest was separated from non-forest using a Band 2 (B2) threshold, where the darkest pixels corresponded to forest [45]. Further separation of forest from green herbaceous cover was possible by using a Tasseled-Cap Greenness (TCG) threshold, where greater TCG values represented green herbaceous cover. B2 and TCG thresholds that maximized classification accuracy were chosen to separate non-forest and forest pixels. Forested pixels were then classified as undisturbed or disturbed using B54A or NBRA thresholds that maximized classification accuracy of undisturbed and disturbed forest classes. Classification accuracy was assessed using high-resolution imagery as reference data and confusion matrices [46].

### 2.6. Prediction of Percent Mortality with Random Forest Modeling

Following an approach similar to that of Meddens and Hicke [31], we developed models predicting percent tree mortality, as determined from aggregated high-resolution classifications, from Landsat variables (Table 2). We chose to use nonparametric Random Forest (RF) modeling [47,48] to avoid possible violations of normal linear regression [49]. In order to give various mortality severities equal weight in RF models, we took equal-sized pixel samples from 10% mortality classes of 0%–10%, 10%–20%, 20%–30%, etc., and combined samples for modeling. We eliminated one variable from highly correlated ( $r > 0.9$ ) variable pairs; the variable that was least correlated with percent mortality, the response variable, was eliminated from correlated pairs. The 'rf.modelSel' function of the 'rfUtilities' package in R was then used to select the best model [50]. The 'rf.modelSel' function creates scaled variable importance scores for each variable, and then tests models that include variables above various importance thresholds; the model that explains the most variation in the response variable with the fewest predictor variables is selected as best. We developed four RF models total; one model for each study area and a general model combining an equal number of samples from each study area (500 observations from each study area for a total of 1500 observations). Ten-fold cross-validation implemented in the 'caret' package of R [51] was used to assess RF model performance in predicting new observations.

Final RF models predicting percent tree mortality for each study area were applied to Landsat time series (1984–2018) predictor variable grids that were 1x1 degrees in size and centered on study areas (Figure 1). Models were applied to pixels classified as disturbed in both the current and following year because we assumed, like Meddens and Hicke [31], that Landsat did not detect initial low-level mortality typical of insect outbreak outset. Pixels classified as non-forest or undisturbed were assigned a value of zero. Pixels that burned, as indicated by MTBS fire perimeter polygons [52], as well as pixels where timber harvest was documented [53], were also assigned a value of zero. We created annual grids of new mortality by subtracting mortality grids from the mortality grid of the previous year. Model application was done with the 'raster' package in R [54].

### 2.7. Comparison with Insect and Disease Aerial Survey Data

We compared total annual mortality area across 1x1 degree extents as estimated by our RF models with annual estimates of total mortality area from USDA insect and disease survey (IDS) polygon data [55], and visually compared Landsat-derived and IDS estimates of tree mortality severity. IDS aerial surveyors estimated mortality severity in terms of trees per acre (TPA) prior to 2016, although some USFS Regions adopted the percent mortality metric as early as 2012. To convert legacy TPA estimates to percent mortality so that total mortality area within IDS polygons could be computed, we used two methodologies: Egan et al. [56], which provides conservative estimates of mortality severity [38], and the methodology of Meddens et al. [57], which provides more liberal mortality

severity estimates. The methodology of Egan et al. [56], which utilizes the relationship between surveyed field TPA and percent mortality plot data to adjust IDS TPA estimates, assigns percent mortality values of 5%, 20%, and 65% to IDS polygons having TPA estimates from 0 to 9.9, 10 to 30, and >30, respectively. The methodology of Meddens et al. [57], which is based on a comparison of high-resolution remote sensing data and IDS TPA, estimates percent mortality with the following:

$$PM = TPA \times CA \times 100 \times 13.6, \quad (3)$$

where  $PM$  is percent mortality,  $TPA$  is the legacy trees per acre (TPA) attribute of the polygon and  $CA$  is the species-specific average crown area, in acres, of the recorded tree host [57] (Appendix A); the 13.6 multiplier compensates for IDS underestimation bias for most tree species/damage agent combinations [57,58]. IDS polygons of abiotic (0.6% of polygons) or insect-caused tree mortality without TPA measurements were assigned a TPA value of 2, the median for all IDS polygons. Our aim was to predict and map tree mortality. However, initial comparison of our tree mortality maps with IDS polygons showed that our approach also detected biotic defoliation or mortality caused by defoliation, hence we included IDS polygons representing defoliation damage when validating our Landsat-derived maps with independent IDS polygon data. IDS polygons of defoliator damage were assigned a percent mortality value of 10% [59–61], the median for all IDS polygons after conversion from TPA.

### 3. Results

#### 3.1. Landsat Classification into Non-Forest, Undisturbed Forest, and Disturbed Forest

Overall classification accuracies ranged from 74% to 80% for pixels that contained > 50% of a given class (Tables 3 and A1–A3). We found that using the B2 mean or the B2 mean plus one standard deviation worked well for separating forest from non-forest. TCG thresholds of the mean TCG plus one or two standard deviations further separated forest from green herbaceous cover. B54A consistently separated disturbed from non-disturbed forest with greater accuracy than NBRA, so we used B54A for final classifications. B54A thresholds that maximized class accuracies ranged from 0.165 to 0.307 (Table 3, Figure 3).

**Table 3.** Band 2 (B2), tasseled-cap greenness (TCG), and band 5/band 4 anomaly (B54A) thresholds used to classify non-, disturbed, and undisturbed forest for each study area. B2 and TGC thresholds were used to separate forest from non-forest (values < thresholds corresponded to forest). B54A thresholds were used to separate disturbed from undisturbed forest (values > B54A thresholds indicate disturbed forest). sd = standard deviation.

Study Area	B2 Threshold	TCG Threshold	B54A Threshold	Overall Accuracy (%)
Stanley, ID	0.57 (mean)	1.0 (mean + 1 sd)	0.307	74
Chimney Park, WY	0.50 (mean)	1.1 (mean + 1 sd)	0.265	75
Elk City, ID	0.51 (mean + 1 sd)	1.8 (mean + 2 sd)	0.165	80

#### 3.2. Prediction of Percent Tree Mortality with Random Forest Modeling

Ten-fold cross-validated RF models explained 61% to 68% of the variation in percent mortality (Table 4, Figure 4). TCB, NDVI, and NBR were the most important variables in RF models for the Stanley, Chimney Park, and Elk City study areas, respectively. TCG and B54A were selected as predictor variables in all study areas. B5, NBR, and TCW were selected as predictor variables in two study areas. B54A and NBR were the most important variables in the general model. Spatial patterns of tree mortality severity as predicted by Landsat variables matched those of high-resolution imagery (Figure 5).

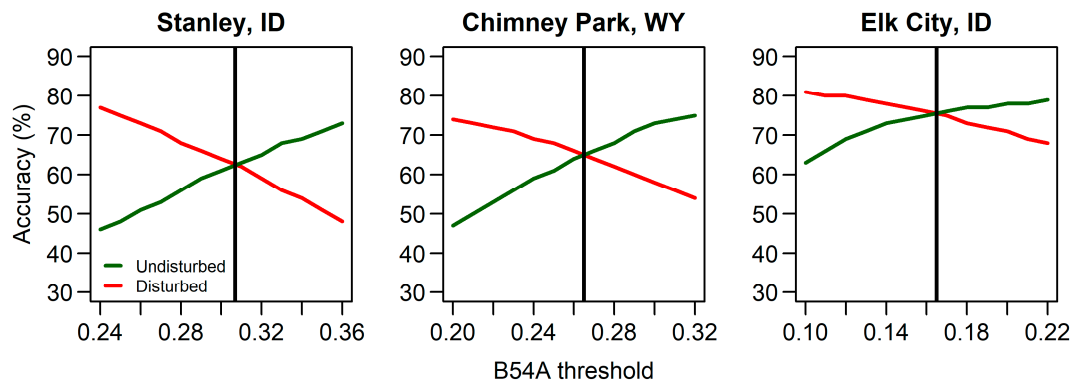


**Figure 3.** Classification accuracies of undisturbed and disturbed forest classes for various band 5/band 4 anomaly (B54A) values. Vertical lines give B54A thresholds that maximized classification accuracy for disturbed and undisturbed forest in each study area.

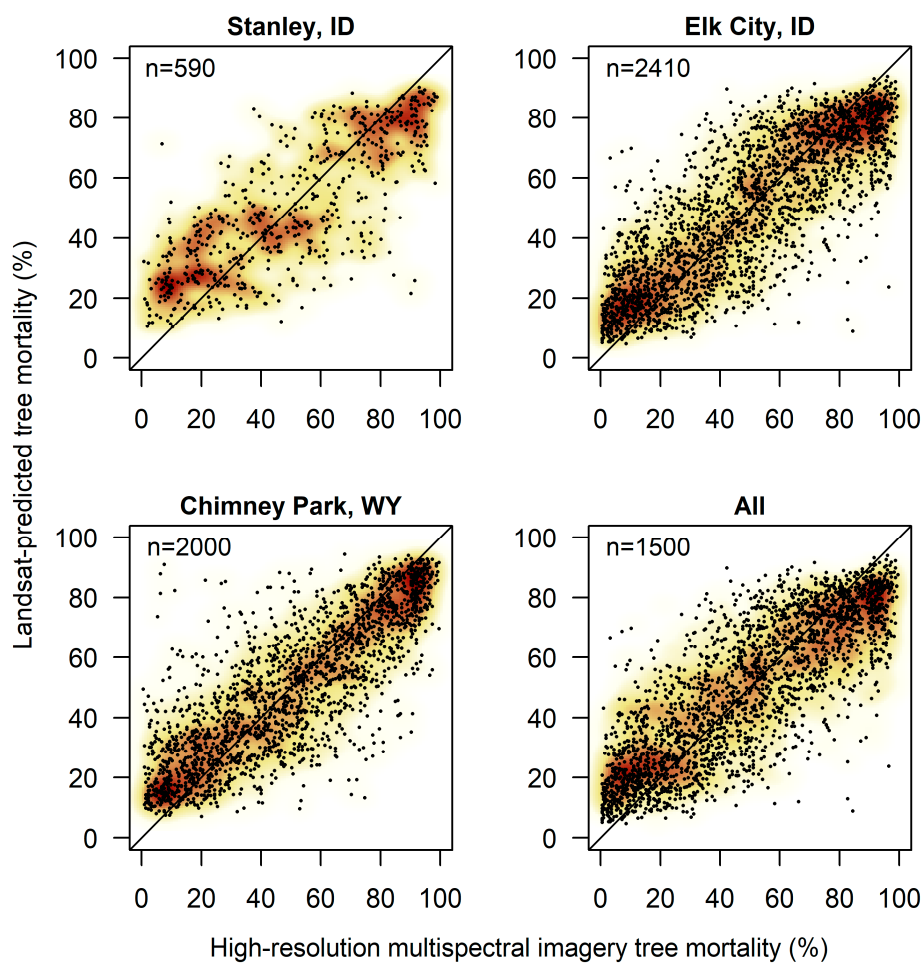


**Figure 4.** Percent tree mortality as observed by high-resolution multispectral imagery versus percent tree mortality as predicted by Landsat variables via cross-validated random forest models. High-resolution multispectral imagery for Stanley, Chimney Park, and Elk City was digital aerial orthophotography, QuickBird, and WorldView-2, respectively.

**Table 4.** Model performance statistics and selected variables and their importance for cross-validated Random Forest models predicting percent mortality from Landsat variables. PVE = percent variance explained; MBE = mean bias error; RMSE = root mean squared error, PRMSE = percent root mean squared error; MIR = model improvement ratio, where values of zero indicate less important and values of one indicate most important; B1 = band 1; B5 = band 5; NBR = normalized burn ratio; NDVI = normalized difference vegetation index; TCB = tasseled-cap brightness; TCG = tasseled-cap greenness; TCW = tasseled-cap wetness; B54A = band 5/band 4 anomaly from undisturbed mean.

Study Area	PVE	MBE	RMSE	PRMSE	Selected Variables (MIR)
Stanley, ID	60.6	-0.11	17.5	35.1	TCB(1.0), B5(0.7), TCG(0.6), TCW(0.4), B1(0.4), B54A(0.2), NDVI(0.2)
Chimney Park, WY	66.4	0.03	16.4	32.8	NDVI(1.0), TCG(0.6), TCW(0.4), B54A(0.4)
Elk City, ID	67.5	-0.04	16.3	32.8	NBR(1.0), B54A(0.4), TCG(0.3), B5(0.2)
All	61.0	-0.14	17.9	35.9	B54A(1.0), NBR(0.6), B2(0.4), B1(0.3), TCG(0.3), TCW(0.3), B5(0.2)

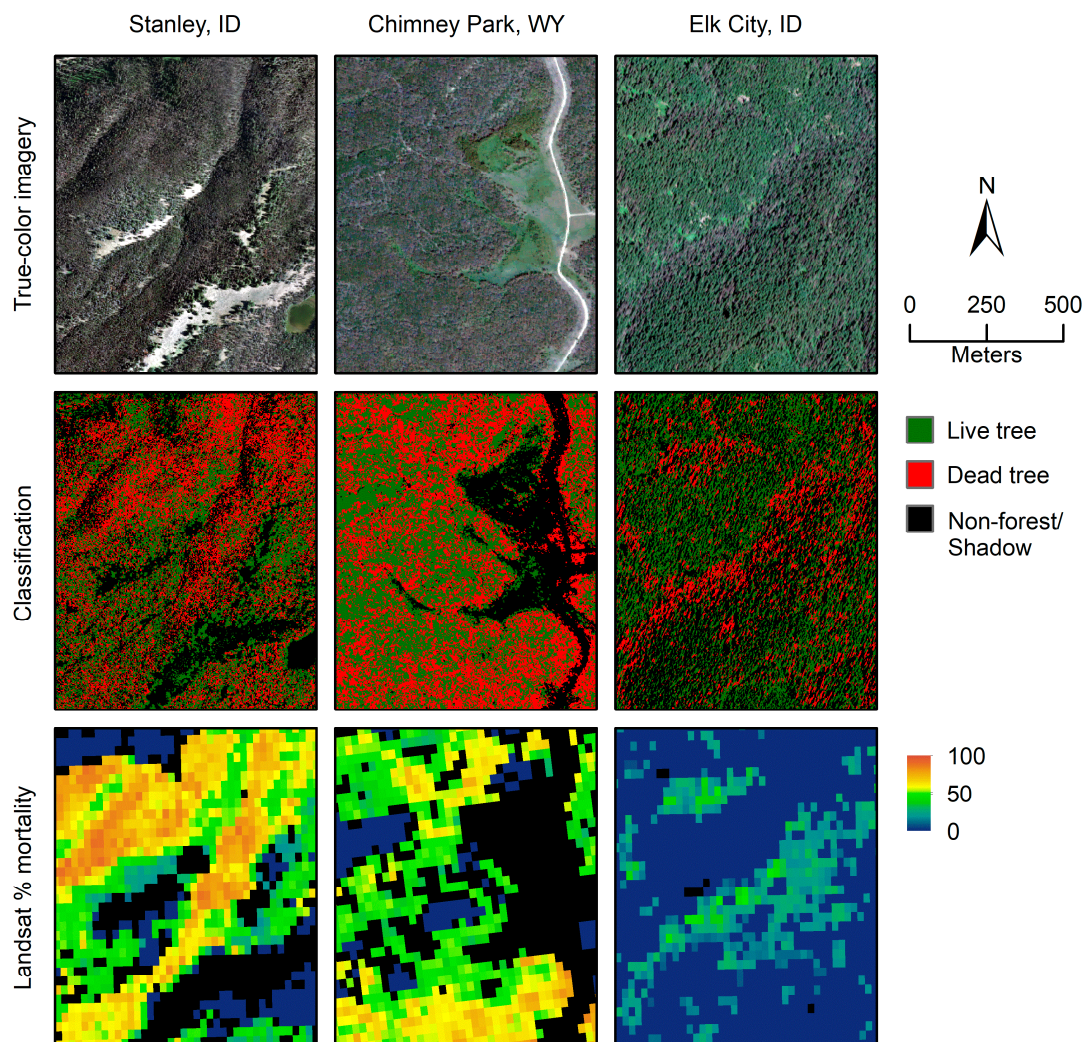


**Figure 5.** Comparison of true-color high-resolution imagery, high-resolution classifications, and percent mortality as estimated by Landsat variables in random forest (RF) models.

### 3.3. Comparison of Landsat-Derived Percent Tree Mortality Maps with Aerial Survey Data

Annual trends of total mortality area as predicted by Landsat were generally similar to those of IDS, with some discrepancies (Figure 6). In Stanley, both Landsat and IDS detected elevated levels of tree mortality from 1985 to 1994, a period of low tree mortality from 1995 to 2001, and elevated levels of mortality from 2001 to 2017. A large defoliation event was documented by IDS in 2015; Landsat also detected tree damage in the same area, but with less total area (Figure 7B).

In Chimney Park, both Landsat and IDS detected little or no tree mortality until 2005 and a large mortality event from 2005 to 2012 (Figure 6). In 2011, at the peak of tree mortality, IDS estimated greater total mortality area (52 to 112 kha), than Landsat (24 kha).

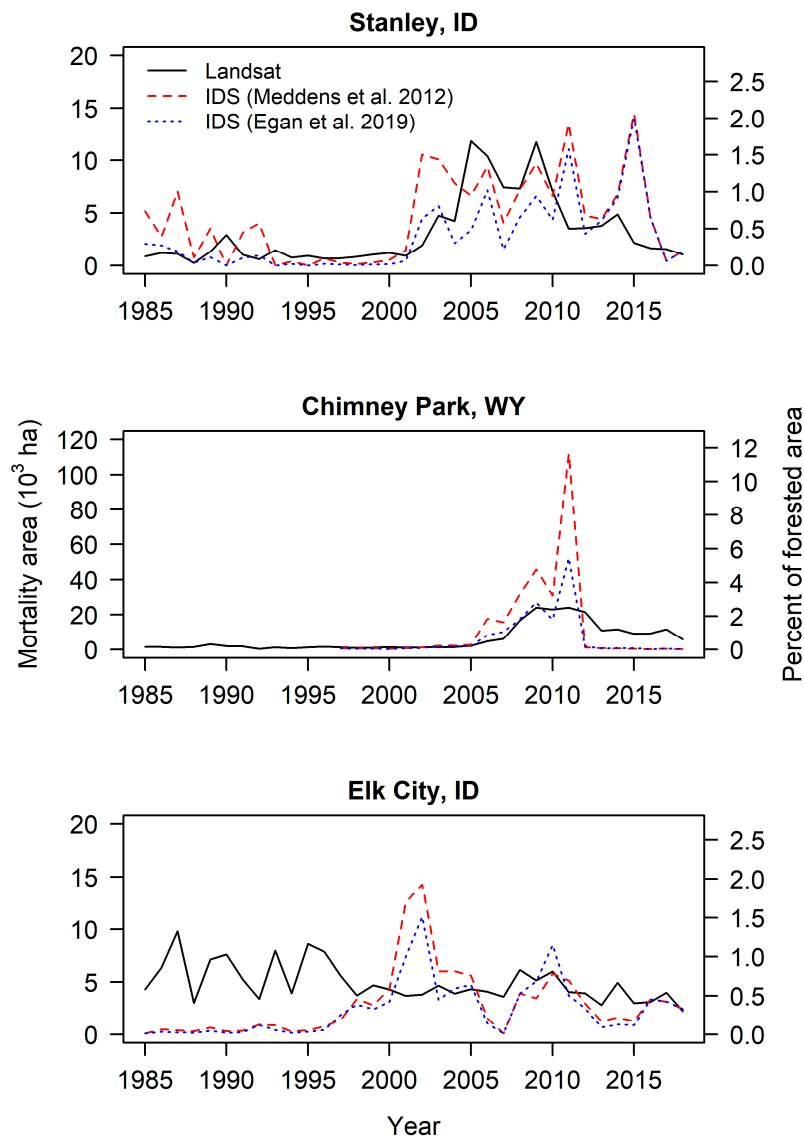


**Figure 6.** Annual estimates of total mortality area across  $1 \times 1$  degree extents from Landsat and insect and disease survey (IDS) polygon data. Wilderness areas, where IDS surveys are conducted infrequently, were excluded.

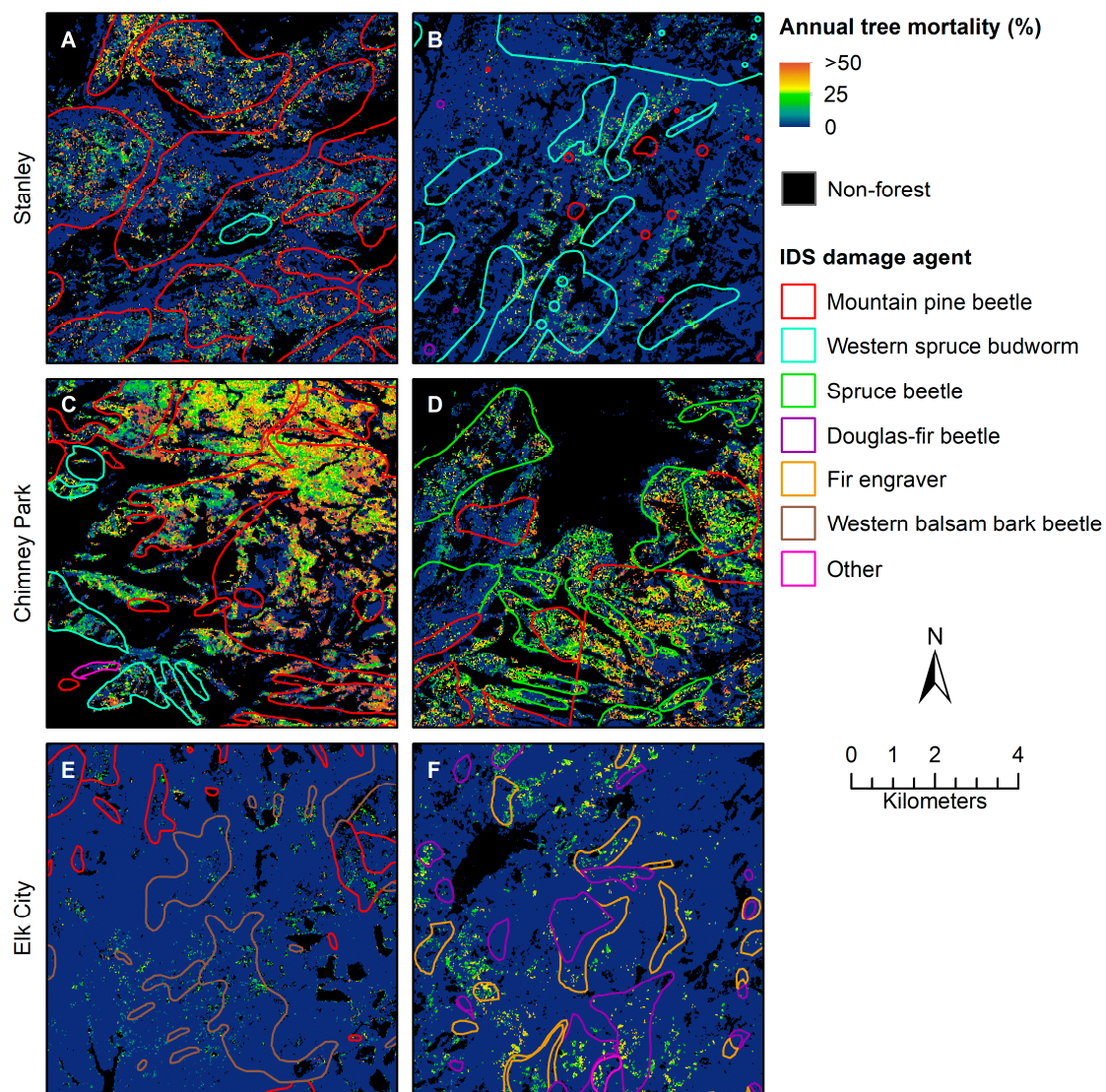


**Figure 7.** Comparison of annual maps of Landsat-derived percent tree mortality and insect and disease survey (IDS) polygon data from various insect agents. Panels show: (A) moderate forest mortality caused by mountain pine beetles in the Stanley study area in 2008; (B) low forest mortality caused by Western spruce budworms in the Stanley study area in 2015; (C) severe forest mortality caused by mountain pine beetles and Western spruce budworms in the Chimney Park study area in 2008; (D) moderate forest mortality caused by spruce and mountain pine beetles in the Chimney Park study area in 2011; (E) low forest mortality caused by Western balsam bark and mountain pine beetles in the Elk City study area in 2001; and (F) low forest mortality caused by Douglas-fir and fir engraver beetles in the Elk City study area in 2017.

Annual trends of total mortality area were most dissimilar between Landsat and IDS in Elk City (Figure 6); Landsat detected continuous mortality levels of 2–10 kha yr<sup>-1</sup> throughout the entire time series (1984 to 2018), whereas IDS did not show elevated tree mortality levels >1 kha yr<sup>-1</sup> until 1997. IDS showed a peak in mortality of 7–14 kha yr<sup>-1</sup> in 2001 and 2002; Landsat detected mortality in the same vicinity, but at lower levels of 4–5 kha yr<sup>-1</sup>. Although annual trends differed, overall mortality levels ranged from 0.1–4 kha yr<sup>-1</sup> for both Landsat and IDS throughout the time series, and Landsat and IDS trends post-2002 tracked each other (Figure 6).

Visual comparison of Landsat-derived maps of tree mortality with IDS polygons generally showed good agreement for a variety of insect agents, especially for moderate and severe forest mortality (Figure 7). Agreement was less apparent for low forest mortality; Landsat often detected forest

disturbance in and around the vicinity of low severity IDS polygons, but not always (Figure 7B,E,F). Although tree mortality caused by fires and harvest, as well as non-forest, were masked, Landsat maps also showed mortality outside IDS polygons (Figure 7E,F). Both the Stanley and Elk City  $1 \times 1$  degree study areas contained large portions of wilderness areas in which Landsat maps revealed substantial unsurveyed tree mortality.

#### 4. Discussion

We estimated insect-caused tree mortality caused by a variety of mortality agents across three large areas for the years 1984 to 2018 using Landsat time series analysis. We separated non-forest, undisturbed, and disturbed forest with overall accuracies of 74% to 80% and explained 61% to 68% of the variation in percent tree mortality using Landsat variables. Similar to others, we found the Landsat shortwave-infrared to near-infrared ratio (B54) index to be a good indicator of change in coniferous forest [31,62,63]. The B54 index was likely sensitive to changes in forest structure caused by forest mortality, rather than directly sensing changes to vegetation physiology. For our application, the detection of insect-caused canopy disturbance, B54 outperformed NBR, another popular index for documenting forest change. However, NBR, as well as NDVI and Landsat Tasseled-Cap variables, were still found to be important predictors of the degree of insect-caused forest decline. Rates of forest disturbance that we estimated within our study areas (0.1% to 3% of forest area  $\text{yr}^{-1}$ ) were similar to the national estimates of Cohen et al. [64] (1.5% to 4.5% of forest area  $\text{yr}^{-1}$ ).

We found GEE [25] and the preprocessing functions of the LandTrendr implementation in GEE [26] to be powerful tools for simplifying the processing of Landsat time series data. Before GEE, the task of preprocessing and managing Landsat time series data required significant resources and time. What required days or weeks of work can now be completed in hours with the functions available in the LandTrendr implementation of GEE, which we found to be simple to understand and execute. The simplicity and efficiency of GEE makes the application of our method across large areas feasible.

RF modeling provided several benefits over linear modeling. First, RF allowed for nonlinear relationships between response and predictor variables. Although many of the relationships between our response variable, percent tree mortality, and Landsat predictor variables were approximately linear, some, particularly B54A, were nonlinear. Second, RF modeling is better suited to modeling continuous percent tree mortality, which can be zero-inflated, i.e., having many values near zero. Zero-inflated data can result in heteroskedastic variance of errors, a violation of normal linear regression [49]. Third, the RF algorithm partitions data into training and evaluation datasets internally. Although we performed ten-fold cross-validation to rigorously evaluate our RF models, we found that model diagnostics of cross-validated models were nearly identical to model diagnostics of non-cross-validated models, suggesting that cross-validation was not necessary and the out-of-bag estimate of error provided by RF was sufficient.

Our methodology has the potential to be applied across large spatial extents. The B2 and TCG thresholds that we used to separate forest from non-forest, as well as the B54A threshold values that we used to separate undisturbed from disturbed forest were comparable across our three study areas (Table 3). In addition, our general RF model combining observations from all study areas performed similarly to RF models of individual study areas (Table 4, Figure 4). This suggests that we could apply this methodology across a large region, such as an entire wilderness area, national forest, state, or Forest Service Region. However, caution should be used when applying algorithms and models outside areas where those models were calibrated, as accuracy might decrease in new areas [63,65]. The use of several calibration sites distributed across the larger area of interest, as well as applying algorithms and models only within similar forest types, would help to minimize inappropriate extrapolation outside calibration areas. Few previous studies have applied Landsat time series analysis for the detection of insect-caused tree mortality across large study areas [27,31,34].

Detection of lower-severity forest disturbance with Landsat remains a challenge. Insect-caused tree mortality usually occurs gradually and at lower levels relative to fire or harvest, making it more challenging

to detect with moderate-resolution satellites. Numerous previous studies have shown that Landsat time series analysis can be used to detect high-severity forest disturbance, where most trees within a 30-m pixel are disturbed, with high accuracy [30,32,49,66]. However, lower-severity disturbance, where fewer trees are disturbed within a 30-m pixel, is detected with less accuracy [30,63,66]. Although we did not specifically examine classification accuracy by disturbance severity, comparison of our Landsat-derived maps with IDS polygons showed that low-severity disturbance as detected by IDS surveyors was not always detected with our Landsat time series analysis, as expected.

Comparison of our Landsat-derived mortality maps with IDS showed some discrepancies, especially in areas of low tree mortality (Figures 6 and 7). However, IDS data are a fundamentally different, vector-based representation of disturbance, so differences are expected. For example, IDS showed a large amount of defoliator-caused tree damage in our Stanley study area in 2015, while Landsat showed much less total area affected (Figure 6). Examination of IDS polygons within a geographic information system (GIS) showed that IDS polygons were large and highly generalized (Figure 7B). Our Landsat-derived maps detected damage in the same areas, but perhaps more precisely. Meigs et al. [34] made a similar observation that IDS polygons are a generalization of damage area that can exaggerate overall area affected, whereas Landsat methods can give more resolved damage estimates at 30-m resolution. So, while our estimates of low-level damage did not always agree with IDS polygons, Landsat representations of low-level tree damage, when detected, are likely more accurate representations of diffuse tree damage than large generalized IDS polygons.

Another notable difference between our Landsat-derived maps and IDS was in the Elk City study area for the years before 1997, where Landsat detected considerable disturbance and IDS showed little. This discrepancy could be caused by limited IDS survey coverage in the 1980s and 1990s, when IDS flights often targeted specific insect agents and some areas were missed on a regular basis. We could not verify this because no information on survey extent was available for IDS data prior to 1997. Our Landsat methodology could have also detected non-insect-related forest disturbance, such as undocumented forest harvest, small fires, or forest decline such as that caused by drought [64]. Indeed, Landsat identified considerable mortality in 1987, the driest year of the years 1980 to 2018 in the Elk City vicinity. Although we masked areas of documented forest harvest, many of the areas identified as being disturbed in the Elk City area prior to 1997 occurred adjacent to areas of timber harvest, particularly along the edges of harvested areas. This highlights one limitation of our approach, that beyond masking large burns and documented harvest with ancillary data, disturbance is not separated by type.

Attributing causes of forest change with satellite time series analysis is a topic of current research [27], where others have made some progress. Senf et al. [67] successfully distinguished between mountain pine beetle mortality and Western spruce budworm damage in British Columbia, Canada using LandTrendr-derived spectral trajectories. Meigs et al. [34] used IDS polygons as ancillary information for distinguishing between forest damage caused by mountain pine beetles and Western spruce budworms. Cohen et al. [64] used TimeSync [68] and ancillary datasets to distinguish harvest and fire from forest decline across the United States. Oeser et al. [69] distinguished between windthrow, bark beetles, and harvest in central Europe with intra-annual Landsat time series analysis. Vogeler et al. [70] distinguished various types of forest disturbance in Minnesota, USA using Landsat time series analysis. Future work could implement similar approaches that use spectral trajectory differences or incorporate ancillary data to further distinguish tree mortality by type.

## 5. Conclusions

We estimated continuous insect-caused tree mortality in three study areas in the Western United States that have experienced recent forest insect outbreaks, and generated maps of continuous tree mortality estimates across large extents for the years 1984 to 2018 for a variety of insect mortality agents. We adapted the previously developed methods of Meddens et al. by using Google Earth Engine (GEE) to pre-process Landsat imagery, and developing nonparametric Random Forest models

to predict percent tree mortality. GEE simplified the preprocessing of Landsat time series imagery, making the application of these methods across large spatial extents and the Landsat satellite time record feasible and useful.

**Author Contributions:** Conceptualization, B.C.B., A.T.H., A.J.H.M., J.M.E. and C.L.J.; methodology, B.C.B. and A.J.H.M.; software, B.C.B.; validation, B.C.B.; formal analysis, B.C.B.; investigation, B.C.B.; resources, A.T.H., J.M.E. and C.L.J.; data curation, B.C.B.; writing—original draft preparation, B.C.B.; writing—review and editing, B.C.B., A.T.H., A.J.H.M., J.M.E. and C.L.J.; visualization, B.C.B.; supervision, A.T.H., J.M.E. and C.L.J.; project administration, B.C.B., A.T.H., A.J.H.M., J.M.E. and C.L.J.; funding acquisition, B.C.B., A.T.H., A.J.H.M., J.M.E. and C.L.J. All authors have read and agreed to the published version of the manuscript.

**Funding:** This research was funded by the USDA Forest Service Special Technology Development Program (STDP), grant no. 19-JV-11221633-189. A.M. was partly funded by the USDA Forest Service Western Wildland Environmental Threat Assessment Center (WWETAC), agreement no. 18-CR-11221633-109. B.B. was partly funded by the National Science Foundation EPSCoR Program, award number EPS-0814387.

**Acknowledgments:** We thank Anthony Martinez, Lucca Schoenthaler, Gabriel Prata, Nuria Sanchez, and Ryan McCarley for helping with fieldwork. QuickBird and WorldView-2 copyright notice: © 2011, 2018 DigitalGlobe, Inc., Longmont CO USA 80503. DigitalGlobe and the DigitalGlobe logos are trademarks of DigitalGlobe, Inc. The use and/or dissemination of this data and/or of any product in any way derived there from are restricted. Unauthorized use and/or dissemination is prohibited. The QuickBird and WorldView-2 imagery used in this study was obtained through the NextView license agreement.

**Conflicts of Interest:** The authors declare no conflict of interest.

## Appendix A

**Table A1.** Confusion matrix describing Landsat classification accuracy of the Stanley, ID study area for aggregated high-resolution pixels that were >50% pure. Overall classification accuracy was 74% (n = 12,432 pixels).

		Aggregated High-Resolution Classification			
		Non-Forest	Undisturbed	Disturbed	Precision (%)
Landsat classification	Non-forest	3988	532	124	86
	Undisturbed	116	2670	1450	63
	Disturbed	40	942	2570	72
	Recall (%)	96	64	62	

Shaded cells indicate correctly classified pixels.

**Table A2.** Confusion matrix describing Landsat classification accuracy of the Chimney Park, WY study area for aggregated high-resolution pixels that were >50% pure. Overall classification accuracy was 75% (n = 100,626 pixels).

		Aggregated High-Resolution Classification			
		Non-Forest	Undisturbed	Disturbed	Precision (%)
Landsat classification	Non-forest	32226	4693	5578	76
	Undisturbed	890	21787	6106	76
	Disturbed	426	7062	21858	74
	Recall (%)	96	65	65	

Shaded cells indicate correctly classified pixels.

**Table A3.** Confusion matrix describing Landsat classification accuracy of the Elk City, ID study area for aggregated high-resolution pixels that were >50% pure. Overall classification accuracy was 80% (n = 16,116 pixels).

		Aggregated High-Resolution Classification			
		Non-Forest	Undisturbed	Disturbed	Precision (%)
Landsat classification	Non-forest	4814	1028	843	72
	Undisturbed	418	4061	472	82
	Disturbed	140	283	4057	91
	Recall (%)	90	76	76	

## References

- Allen, C.D.; Macalady, A.K.; Chenchouni, H.; Bachelet, M.; McDowell, N.; Vennetier, M.; Kitzberger, T.; Rigling, A.; Breshears, D.D.; Hogg, T.; et al. A global overview of drought and heat-induced tree mortality reveals emerging climate change risks for forests. *For. Ecol. Manag.* **2010**, *259*, 660–684. [[CrossRef](#)]
- Brunelle, A.; Rehfeldt, G.E.; Bentz, B.; Munson, A.S. Holocene records of Dendroctonus bark beetles in high elevation pine forests of Idaho and Montana, USA. *For. Ecol. Manag.* **2008**, *255*, 836–846. [[CrossRef](#)]
- Raffa, K.F.; Aukema, B.H.; Bentz, B.J.; Carroll, A.L.; Hicke, J.; Turner, M.G.; Romme, W.H. Cross-scale Drivers of Natural Disturbances Prone to Anthropogenic Amplification: The Dynamics of Bark Beetle Eruptions. *Bioscience* **2008**, *58*, 501–517. [[CrossRef](#)]
- Bentz, B.J.; Régnière, J.; Fettig, C.J.; Hansen, E.M.; Hayes, J.L.; Hicke, J.A.; Kelsey, R.G.; Negrón, J.F.; Seybold, S.J. Climate Change and Bark Beetles of the Western United States and Canada: Direct and Indirect Effects. *Bioscience* **2010**, *60*, 602–613. [[CrossRef](#)]
- Seidl, R.; Thom, D.; Kautz, M.; Martin-Benito, D.; Peltoniemi, M.; Vacchiano, G.; Wild, J.; Ascoli, D.; Petr, M.; Honkaniemi, J.; et al. Forest disturbances under climate change. *Nat. Clim. Chang.* **2017**, *7*, 395–402. [[CrossRef](#)] [[PubMed](#)]
- Pugh, E.; Small, E. The impact of pine beetle infestation on snow accumulation and melt in the headwaters of the Colorado River. *Ecolhydrology* **2011**, *5*, 467–477. [[CrossRef](#)]
- Mikkelsen, K.M.; Bearup, L.; Maxwell, R.M.; Stednick, J.D.; McCray, J.E.; Sharp, J.O. Bark beetle infestation impacts on nutrient cycling, water quality and interdependent hydrological effects. *Biogeochemistry* **2013**, *115*, 1–21. [[CrossRef](#)]
- Hicke, J.; Meddens, A.J.H.; Allen, C.D.; Kolden, C.A. Carbon stocks of trees killed by bark beetles and wildfire in the western United States. *Environ. Res. Lett.* **2013**, *8*, 035032. [[CrossRef](#)]
- Saab, V.A.; Latif, Q.S.; Rowland, M.M.; Johnson, T.N.; Chalfoun, A.D.; Buskirk, S.; Heyward, J.E.; Dresser, M.A. Ecological Consequences of Mountain Pine Beetle Outbreaks for Wildlife in Western North American Forests. *For. Sci.* **2014**, *60*, 539–559. [[CrossRef](#)]
- Dhar, A.; Parrott, L.; Heckbert, S. Consequences of mountain pine beetle outbreak on forest ecosystem services in western Canada. *Can. J. For. Res.* **2016**, *46*, 987–999. [[CrossRef](#)]
- Edburg, S.L.; Hicke, J.A.; Lawrence, D.; Thornton, P.E. Simulating coupled carbon and nitrogen dynamics following mountain pine beetle outbreaks in the western United States. *J. Geophys. Res. Space Phys.* **2011**, *116*. [[CrossRef](#)]
- Bright, B.C.; Hicke, J.; Meddens, A.J.H. Effects of bark beetle-caused tree mortality on biogeochemical and biogeophysical MODIS products. *J. Geophys. Res. Biogeosci.* **2013**, *118*, 974–982. [[CrossRef](#)]
- Dietze, M.C.; Matthes, J.H. A general ecophysiological framework for modelling the impact of pests and pathogens on forest ecosystems. *Ecol. Lett.* **2014**, *17*, 1418–1426. [[CrossRef](#)] [[PubMed](#)]
- Krist, F.J., Jr.; Ellenwood, J.R.; Woods, M.E.; McMahan, A.J.; Cowardin, J.P.; Ryerson, D.E.; Sapio, F.J.; Zweifel, M.O.; Romero, S.A. *2013–2027 National Insect and Disease Forest Risk Assessment*; FHTET-14-01; U.S. Department of Agriculture Forest Service, Forest Health Technology Enterprise Team: Fort Collins, CO, USA, 2014; 199p.
- USDA Forest Service. *Major Forest Insect and Disease Conditions in the United States: 2015*; FS-1093; Forest Health Protection: Washington, DC, USA, 2017; 56p.

16. Hart, S.J.; Schoennagel, T.; Veblen, T.T.; Chapman, T.B. Area burned in the western United States is unaffected by recent mountain pine beetle outbreaks. *Proc. Natl. Acad. Sci. USA* **2015**, *112*, 4375–4380. [[CrossRef](#)] [[PubMed](#)]
17. Buotte, P.C.; Hicke, J.; Preisler, H.K.; Abatzoglou, J.T.; Raffa, K.F.; Logan, J.A. Climate influences on whitebark pine mortality from mountain pine beetle in the Greater Yellowstone Ecosystem. *Ecol. Appl.* **2016**, *26*, 2507–2524. [[CrossRef](#)]
18. Coleman, T.W.; Graves, A.D.; Heath, Z.; Flowers, R.W.; Hanavan, R.P.; Cluck, D.R.; Ryerson, D. Accuracy of aerial detection surveys for mapping insect and disease disturbances in the United States. *For. Ecol. Manag.* **2018**, *430*, 321–336. [[CrossRef](#)]
19. Housman, I.W.; Chastain, R.A.; Finco, M.V. An Evaluation of Forest Health Insect and Disease Survey Data and Satellite-Based Remote Sensing Forest Change Detection Methods: Case Studies in the United States. *Remote Sens.* **2018**, *10*, 1184. [[CrossRef](#)]
20. Banskota, A.; Kayastha, N.; Falkowski, M.J.; Wulder, M.A.; Froese, R.E.; White, J.C. Forest Monitoring Using Landsat Time Series Data: A Review. *Can. J. Remote Sens.* **2014**, *40*, 362–384. [[CrossRef](#)]
21. Huang, C.; Goward, S.N.; Masek, J.G.; Thomas, N.; Zhu, Z.; Vogelmann, J. An automated approach for reconstructing recent forest disturbance history using dense Landsat time series stacks. *Remote Sens. Environ.* **2010**, *114*, 183–198. [[CrossRef](#)]
22. Kennedy, R.E.; Yang, Z.; Cohen, W. Detecting trends in forest disturbance and recovery using yearly Landsat time series: 1. LandTrendr—Temporal segmentation algorithms. *Remote Sens. Environ.* **2010**, *114*, 2897–2910. [[CrossRef](#)]
23. Verbesselt, J.; Hyndman, R.J.; Newnham, G.; Culvenor, D. Detecting trend and seasonal changes in satellite image time series. *Remote Sens. Environ.* **2010**, *114*, 106–115. [[CrossRef](#)]
24. Zhu, Z.; Woodcock, C.E. Continuous change detection and classification of land cover using all available Landsat data. *Remote Sens. Environ.* **2014**, *144*, 152–171. [[CrossRef](#)]
25. Gorelick, N.; Hancher, M.; Dixon, M.; Ilyushchenko, S.; Thau, D.; Moore, R. Google Earth Engine: Planetary-scale geospatial analysis for everyone. *Remote Sens. Environ.* **2017**, *202*, 18–27. [[CrossRef](#)]
26. Kennedy, R.; Yang, Z.; Gorelick, N.; Braaten, J.; Cavalcante, L.; Cohen, W.B.; Healey, S.P. Implementation of the LandTrendr Algorithm on Google Earth Engine. *Remote Sens.* **2018**, *10*, 691. [[CrossRef](#)]
27. Senf, C.; Seidl, R.; Hostert, P. Remote sensing of forest insect disturbances: Current state and future directions. *Int. J. Appl. Earth Obs. Geoinf.* **2017**, *60*, 49–60. [[CrossRef](#)] [[PubMed](#)]
28. Meigs, G.W.; Kennedy, R.E.; Cohen, W. A Landsat time series approach to characterize bark beetle and defoliator impacts on tree mortality and surface fuels in conifer forests. *Remote Sens. Environ.* **2011**, *115*, 3707–3718. [[CrossRef](#)]
29. Townsend, P.A.; Singh, A.; Foster, J.; Rehberg, N.J.; Kingdon, C.C.; Eshleman, K.; Seagle, S.W. A general Landsat model to predict canopy defoliation in broadleaf deciduous forests. *Remote Sens. Environ.* **2012**, *119*, 255–265. [[CrossRef](#)]
30. Meddens, A.J.H.; Hicke, J.; Vierling, L.A.; Hudak, A.T. Evaluating methods to detect bark beetle-caused tree mortality using single-date and multi-date Landsat imagery. *Remote Sens. Environ.* **2013**, *132*, 49–58. [[CrossRef](#)]
31. Meddens, A.J.H.; Hicke, J. Spatial and temporal patterns of Landsat-based detection of tree mortality caused by a mountain pine beetle outbreak in Colorado, USA. *For. Ecol. Manag.* **2014**, *322*, 78–88. [[CrossRef](#)]
32. Assal, T.; Sibold, J.; Reich, R. Modeling a Historical Mountain Pine Beetle Outbreak Using Landsat MSS and Multiple Lines of Evidence. *Remote Sens. Environ.* **2014**, *155*, 275–288. [[CrossRef](#)]
33. Long, J.; Lawrence, R.L. Mapping Percent Tree Mortality Due to Mountain Pine Beetle Damage. *For. Sci.* **2016**, *62*, 392–402. [[CrossRef](#)]
34. Meigs, G.W.; Kennedy, R.E.; Gray, A.N.; Gregory, M.J. Spatiotemporal dynamics of recent mountain pine beetle and western spruce budworm outbreaks across the Pacific Northwest Region, USA. *For. Ecol. Manag.* **2015**, *339*, 71–86. [[CrossRef](#)]
35. Woodward, B.D.; Evangelista, P.H.; Vorster, A. Mapping Progression and Severity of a Southern Colorado Spruce Beetle Outbreak Using Calibrated Image Composites. *Forests* **2018**, *9*, 336. [[CrossRef](#)]
36. Research on Forest Climate Change: Potential Effects of Global Warming on Forests and Plant Climate Relationships in Western North America and Mexico. Available online: <http://charcoal.cnre.vt.edu/climate/> (accessed on 6 April 2020).

37. Bright, B.C.; Hicke, J.A.; Hudak, A.T. Estimating aboveground carbon stocks of a forest affected by mountain pine beetle in Idaho using lidar and multispectral imagery. *Remote Sens. Environ.* **2012**, *124*, 270–281. [[CrossRef](#)]
38. Bright, B.C.; Hudak, A.; Egan, J.; Jorgensen, C.; Rex, F.; Hicke, J.A.; Meddens, A. Using Satellite Imagery to Evaluate Bark Beetle-Caused Tree Mortality Reported in Aerial Surveys in a Mixed Conifer Forest in Northern Idaho, USA. *Forests* **2020**, *11*, 529. [[CrossRef](#)]
39. Meddens, A.J.H.; Hicke, J.; Vierling, L.A. Evaluating the potential of multispectral imagery to map multiple stages of tree mortality. *Remote Sens. Environ.* **2011**, *115*, 1632–1642. [[CrossRef](#)]
40. DigitalGlobe. Absolute Radiometric Calibration: 2016v0, Prepared by Michele, A. Kuester. DigitalGlobe Inc. Headquarters: Westminster, Colorado, USA, 2017, 8p. Available online: [https://dg-cms-uploads-production.s3.amazonaws.com/uploads/document/file/209/ABSRADCAL\\_FLEET\\_2016v0\\_Rel20170606.pdf](https://dg-cms-uploads-production.s3.amazonaws.com/uploads/document/file/209/ABSRADCAL_FLEET_2016v0_Rel20170606.pdf) (accessed on 9 March 2020).
41. Smith, G.M.; Milton, E.J. The use of the empirical line method to calibrate remotely sensed data to reflectance. *Int. J. Remote Sens.* **1999**, *20*, 2653–2662. [[CrossRef](#)]
42. Jensen, J.R.; Lulla, K. Introductory digital image processing: A remote sensing perspective. *Geocarto Int.* **1987**, *2*, 65. [[CrossRef](#)]
43. Roy, D.; Kovalskyy, V.; Zhang, H.; Vermote, E.; Yan, L.; Kumar, S.S.; Egorov, A. Characterization of Landsat-7 to Landsat-8 reflective wavelength and normalized difference vegetation index continuity. *Remote Sens. Environ.* **2016**, *185*, 57–70. [[CrossRef](#)]
44. Anonymous. The R Project for Statistical Computing. Available online: <http://www.r-project.org/> (accessed on 13 February 2012).
45. Huang, C.; Song, K.; Kim, S.; Townshend, J.R.; Davis, P.; Masek, J.; Goward, S.N. Use of a dark object concept and support vector machines to automate forest cover change analysis. *Remote Sens. Environ.* **2008**, *112*, 970–985. [[CrossRef](#)]
46. Congalton, R.G. A review of assessing the accuracy of classifications of remotely sensed data. *Remote Sens. Environ.* **1991**, *37*, 35–46. [[CrossRef](#)]
47. Breiman, L. Random Forests. *Mach. Learn.* **2001**, *45*, 5–32. [[CrossRef](#)]
48. Liaw, A.; Wiener, M. Classification and regression by randomforest. *R News* **2002**, *2*, 18–22.
49. Schwantes, A.M.; Swenson, J.J.; Jackson, R.B. Quantifying drought-induced tree mortality in the open canopy woodlands of central Texas. *Remote Sens. Environ.* **2016**, *181*, 54–64. [[CrossRef](#)]
50. Murphy, M.; Evans, J.; Storfer, A. Quantifying Bufo boreas connectivity in Yellowstone National Park with landscape genetics. *Ecology* **2010**, *91*, 252–261. [[CrossRef](#)]
51. Kuhn, M. Caret: Classification and Regression Training. R Package Version 6.0-86. 2020. Available online: <https://CRAN.R-project.org/package=caret> (accessed on 6 April 2020).
52. Eidenshink, J.; Schwind, B.; Brewer, K.; Zhu, Z.; Quayle, B.; Howard, S. A Project for Monitoring Trends in Burn Severity. *Fire Ecol.* **2007**, *3*, 3–21. [[CrossRef](#)]
53. FSGeodata Clearinghouse, Download National Datasets, Timber Harvest. Available online: <https://data.fs.usda.gov/geodata/edw/datasets.php> (accessed on 31 January 2020).
54. Hijmans, R.J. Raster: Geographic Data Analysis and Modeling. R Package Version 3.0-12. 2020. Available online: <https://CRAN.R-project.org/package=raster> (accessed on 6 April 2020).
55. Insect & Disease Detection Survey (IDS) Data Downloads. Available online: <https://www.fs.fed.us/foresthealth/applied-sciences/mapping-reporting/detection-surveys.shtml> (accessed on 5 December 2019).
56. Egan, J.M.; Kaiden, J.; Lestina, J.; Stasey, A.; Jenne, J.L. *Techniques to Enhance Assessment and Reporting of Pest Damage Estimated with Aerial Detection Surveys*; R1-19-09; US Department of Agriculture, Forest Service, Northern Region, Forest Health Protection: Missoula, MT, USA, 2019; 33p.
57. Meddens, A.J.H.; Hicke, J.; Ferguson, C.A. Spatiotemporal patterns of observed bark beetle-caused tree mortality in British Columbia and the western United States. *Ecol. Appl.* **2012**, *22*, 1876–1891. [[CrossRef](#)]
58. Hicke, J.; Meddens, A.J.H.; Kolden, C.A. Recent Tree Mortality in the Western United States from Bark Beetles and Forest Fires. *For. Sci.* **2016**, *62*, 141–153. [[CrossRef](#)]
59. Collis, D.G.; van Sickle, G.A. Damage Appraisal Cruises in Spruce Budworm Defoliated Stands of Douglas-fir in 1977, Information Report BC-P-19. Fisheries and Environment Canada, Canadian Forest Service, Pacific Forest Research Centre, Victoria, British Columbia, 1978. 8p. Available online: <https://cfs.nrcan.gc.ca/publications?id=1853> (accessed on 6 April 2020).

60. Alfaro, R.I.; Van Sickle, G.A.; Thomson, A.J.; Wegwitz, E. Tree mortality and radial growth losses caused by the western spruce budworm in a Douglas-fir stand in British Columbia. *Can. J. For. Res.* **1982**, *12*, 780–787. [[CrossRef](#)]
61. Powell, D. *Effects of the 1980s Western Spruce Budworm Outbreak on the Malheur National Forest in Northeastern Oregon*; Technical Publication R6-FI&D-TP-12-94; USDA Forest Service, Pacific Northwest Region: Portland, OR, USA, 1994; 176p.
62. Vogelmann, J.; Xian, G.; Homer, C.; Tolk, B. Monitoring gradual ecosystem change using Landsat time series analyses: Case studies in selected forest and rangeland ecosystems. *Remote Sens. Environ.* **2012**, *122*, 92–105. [[CrossRef](#)]
63. Cohen, W.; Yang, Z.; Healey, S.P.; Kennedy, R.E.; Gorelick, N. A LandTrendr multispectral ensemble for forest disturbance detection. *Remote Sens. Environ.* **2018**, *205*, 131–140. [[CrossRef](#)]
64. Cohen, W.B.; Yang, Z.; Stehman, S.V.; Schroeder, T.A.; Bell, D.M.; Masek, J.G.; Huang, C.; Meigs, G.W. Forest disturbance across the conterminous United States from 1985–2012: The emerging dominance of forest decline. *For. Ecol. Manag.* **2016**, *360*, 242–252. [[CrossRef](#)]
65. Cohen, W.B.; Healey, S.P.; Yang, Z.; Stehman, S.V.; Brewer, C.K.; Brooks, E.B.; Gorelick, N.; Huang, C.; Hughes, M.J.; Kennedy, R.E.; et al. How Similar Are Forest Disturbance Maps Derived from Different Landsat Time Series Algorithms? *Forests* **2017**, *8*, 98. [[CrossRef](#)]
66. Goodwin, N.R.; Coops, N.C.; Wulder, M.A.; Gillanders, S.; Schroeder, T.A.; Nelson, T. Estimation of insect infestation dynamics using a temporal sequence of Landsat data. *Remote Sens. Environ.* **2008**, *112*, 3680–3689. [[CrossRef](#)]
67. Senf, C.; Pflugmacher, D.; Wulder, M.A.; Hostert, P. Characterizing spectral–temporal patterns of defoliator and bark beetle disturbances using Landsat time series. *Remote Sens. Environ.* **2015**, *170*, 166–177. [[CrossRef](#)]
68. Cohen, W.; Yang, Z.; Kennedy, R. Detecting trends in forest disturbance and recovery using yearly Landsat time series: 2. TimeSync—Tools for calibration and validation. *Remote Sens. Environ.* **2010**, *114*, 2911–2924. [[CrossRef](#)]
69. Oeser, J.; Pflugmacher, D.; Senf, C.; Heurich, M.; Hostert, P. Using Intra-Annual Landsat Time Series for Attributing Forest Disturbance Agents in Central Europe. *Forests* **2017**, *8*, 251. [[CrossRef](#)]
70. Vogeler, J.C.; Slesak, R.A.; Fekety, P.A.; Falkowski, M.J. Characterizing over Four Decades of Forest Disturbance in Minnesota, USA. *Forests* **2020**, *11*, 362. [[CrossRef](#)]



© 2020 by the authors. Licensee MDPI, Basel, Switzerland. This article is an open access article distributed under the terms and conditions of the Creative Commons Attribution (CC BY) license (<http://creativecommons.org/licenses/by/4.0/>).